Contents lists available at ScienceDirect

Transactions of Nonferrous Metals Society of China

36(2026) 677−693

www.tnmsc.cn

Comparative evaluation of microstructure, mechanical properties, and strengthening mechanisms in cast and selective laser melted AlSi10Mg alloys with direct aging treatment

A. SATHISHKUMAR [a], R. SOUNDARARAJAN [a], S. SIVASANKARAN [b,*], A. RAMESH [c]

[a] Department of Mechanical Engineering, Sri Krishna College of Engineering and Technology, Coimbatore, India;

[b] Department of Mechanical Engineering, College of Engineering, Qassim University, Buraydah 51452, Saudi Arabia;

[c] Department of Mechanical Engineering, Chennai Institute of Technology, Chennai, India

Abstract: The impact of selective laser melting (SLM) and direct aging (DA) heat treatment on the microstructure and mechanical properties of AlSi10Mg alloys was investigated. Microstructural characterization using SEM and EBSD revealed that SLM alloys exhibited a fine-grained cellular structure with α(Al) and Si-enriched phases, whereas cast alloys displayed a coarse eutectic Si morphology. Subsequent DA treatment demonstrated a 9.24% higher yield strength and a 5.56% improvement in ultimate tensile strength of the DA-B AlSi10Mg alloy when compared to the non-heat-treated alloy (NHT-AB), indicating significant improvements due to the DA process. Fracture surface analysis indicated predominantly ductile fracture in SLM alloys, contrasting with mixed ductile−brittle behavior in cast samples. Furthermore, EBSD texture analysis indicated a grain elongation in necked regions of SLM alloys after tensile deformation. The precipitation strengthening significantly contributes to the enhanced strength of the SLM alloys followed by the cell boundary strengthening. These findings highlight the potential of SLM and DA for producing high-performance AlSi10Mg components for aerospace, automotive, and rapid prototyping applications.

Keywords: AlSi10Mg alloy; selective laser melting; direct aging; mechanical properties; strengthening mechanism; EBSD texture analysis

1 Introduction

Lightweight materials play a pivotal role in automotive, aerospace, and marine industries, with aluminum alloys (AAs). The AlSi10Mg alloy is extensively employed in aviation, maritime, and automotive applications due to its superior properties [1]. Traditional liquid metallurgical processes, such as casting, have been conventionally used for AA fabrication, yet they face challenges in meeting contemporary industrial demands [2]. Recently, the additive manufacturing technology (AMT) has revolutionized in modern manufacturing industries for the production of complex engineering components with several features (design flexibility and effective materials utilization) which were difficult to produce in conventional methods [3–7]. The selective laser melting (SLM) stands out as a prominent method for fabricating AAs, particularly the AlSi10Mg alloy [1]. SLM is a specific additive manufacturing process falling under the powder bed fusion (PBF) category. The rapid cooling rate of SLM (10^6−10^8 °C/s) during AlSi10Mg alloy processing, refines the microstructure, enhancing the homogeneity of silicon phase. This is a stark contrast to conventional casting processes, where limited cooling rates (approximately 10^2 °C/s or less)

Corresponding author: *S. SIVASANKARAN, Tel: +966-534810975, E-mail: s.udayar@qu.edu.sa

https://doi.org/10.1016/S1003-6326(25)66990-1

Received 27 May 2024; accepted 27 March 2025

result in coarse eutectic Si phases and hinder microstructure modification [1,8,9].

Recent focus has centered on optimizing SLM parameters and incorporating thermal post-processing for AlSi10Mg alloy. Investigations have revealed that reduced layer thickness (LT) and hatch space (HS) significantly enhance tensile properties, while scan strategy notably impacts fracture toughness in laser powder bed fusion (LPBF)-processed AlSi10Mg [10,11]. Beyond process parameters, particle size distribution (PSD) and Si morphology significantly contribute to the performance of SLM-fabricated AlSi10Mg. Studies have shown that finer PSD and more spherical shapes yield higher part densities and smoother surfaces, ultimately improving the mechanical properties [12]. Furthermore, the high strength of the AlSi10Mg alloy produced via SLM is attributed to multiple strengthening mechanisms, including precipitation or Orowan strengthening, Hall−Petch or cell boundary strengthening, and solid solution strengthening mechanisms [13,14]. The strengthening effect from the eutectic Si phase network, along with the dislocation load-bearing capacity provided by refined dendritic arms, plays a significant role in enhancing the alloy's strength [15]. Additionally, the presence of Si precipitates (Orowan strengthening) and the eutectic cell walls further contribute to the high strength of the SLM-processed AlSi10Mg alloy [16]. Besides, the absence of precipitation strengthening in heat-treated samples results in lower strength at elevated temperatures. During high-temperature treatments including solution heat treatment (SHT), the supersaturated Si precipitates out, reducing the solid solution strengthening, and the disappearance of cell boundaries diminishes the contribution of cell boundary strengthening [17,18].

Various thermal treatments significantly influence the microstructural features and performance of AlSi10Mg alloy produced through SLM [19−23]. For example, SHT at 520 °C induced Si particle coarsening and reduced hardness in SLM-produced AlSi10Mg alloy [18]. Similarly, stress relief (SR) at 300 °C for 2 h and SHT at 450 °C/550 °C for 2 h, followed by artificial aging route (AAR) at 180 °C for 12 h, were applied to as-fabricated AlSi10Mg alloy and it was found that there is an increase in the Si particle dimensions with SHT, especially above 450 °C, correlated with a decline in hardness and tensile strength [24]. Diverse thermal processes, including stress relieving and high-temperature annealing [25], showed reduced yield strength (YS) and ultimate tensile strength (UTS) but increased elongation at failure [26]. Elevated temperature treatments softened the material and in turn decreased the hardness, UTS, and ultimate compressive strength [27]. In contrast, a modified T5 treatment (200 °C for 2 h) exhibited improved hardness and UTS due to nano-scale Si precipitations [28]. Similarly, the mechanical performance of the LPBF-processed A357 alloy, optimized through T6 and direct aging (DA) heat treatments, exhibits enhanced strength in the DA-treated alloy, credited to partial residual stress relief [29]. These findings highlight the nuanced impact of thermal treatments on the AlSi10Mg alloy's properties, providing insights for tailored material performance in SLM applications.

Previous researches on the SLM-processed AlSi10Mg alloy at elevated temperatures resulted in coarsening and dissolving the cellular eutectic Si phase [30−32], consequently diminishing the mechanical performance [17,33−42]. Consolidated mechanical performances of AlSi10Mg alloy subjected to various thermal treatments were reported in the previous studies. However, the impact of DA treatment coupled with air cooling on the tensile behavior and strengthening mechanisms in cast and SLM-produced AlSi10Mg alloys remains unexplored. The current research work aims to fill this gap, investigating the effects of DA heat treatment on the tensile behavior of AlSi10Mg alloys produced through casting and SLM. Additionally, the study delves into the strengthening mechanisms influencing the strength of cast, SLM-processed and direct-aged AlSi10Mg alloys. The failure mechanism is scrutinized through SEM, and EBSD texture analysis is conducted on the fractured surface at the necked region of the tensile-tested samples for a comprehensive understanding.

2 Experimental

In this study, two distinct manufacturing techniques, namely, casting and SLM, were utilized to process the AlSi10Mg alloy.

2.1 Conventional casting process

To produce cast samples, AlSi10Mg alloy (sourced from Coimbatore Metal Mart, India) was

melted in a steel crucible (Swam Equipment's, India) at 700 °C. An argon-inert gas atmosphere was maintained to prevent the molten AlSi10Mg alloy from oxidizing. The elemental constituents are detailed in Table 1. Melting continued until a uniform liquid phase was attained. Slag removal powder was used to eliminate the impurities, and the molten metal was cast in a preheated H13 metallic die at 255 °C, creating non-heat treated as-cast (NHT-AC) alloy. Figure 1(a) illustrates the schematic view of the casting process, yielding specimens with 50 mm in diameter and 100 mm in length for this investigation.

2.2 Selective laser melting process

The non-heat-treated as-built (NHT-AB) alloy was produced using recycled AlSi10Mg powder in an SLM 280 HL 2.0 system. The elemental constituents are detailed in Table 2 (DIN-EN-1706 standard). SEM morphology in Fig. 2(a) displays a mixture of spherical and elongated particles in the recycled AlSi10Mg powder, with an average size of 30 μm (Fig. 2(b)). Prior to processing, the powders were sieved, and a 60 °C temperature treatment was applied to removing moisture and minimizing oxygen presence. Figure 1(b) illustrates the experimental setup and schematic of the SLM used to create the fishbone-shaped tensile samples (100 mm × 10 mm × 5 mm). The process parameters (Table 3) were selected based on experimental trials and suggestions from the supplier (SLM solutions) to minimize crystallographic texture and optimize laser vector alignment between layers. An argon inert gas atmosphere, with a residual oxygen concentration of 0.1%, was maintained throughout the process.

2.3 Direct aging heat treatment process

Utilizing traditional casting and SLM process, the AlSi10Mg alloy was successfully fabricated, yielding test samples. Two batches, NHT-AC and NHT-AB, were prepared from casting and SLM, respectively. The second batch underwent a DA thermal treatment (180 °C for 6 h) and air cooling, resulting in direct-aged (DA-C) and direct-aged built (DA-B) samples. Muffle furnace (Thermotech Engineering, India) was used for the DA thermal treatment. With four sets of samples from casting, SLM, and DA treatments, a comprehensive evaluation was conducted to correlate microstructural changes with the metallurgical and tensile characteristics of AlSi10Mg alloy specimens.

2.4 Metallographic investigations

The microstructure of 10 mm × 10 mm × 5 mm

Table 1 Elemental constituents of AlSi10Mg alloy (wt.%)

Condition	Si	Mg	Fe	Cu	Zn	Ti	Mn	Ni	Pb	Sn	Al
Standard	9−11	0.2−0.45	<0.55	<0.05	<0.10	<0.15	<0.45	<0.05	<0.05	<0.05	Bal.
Measured	9.312	0.317	0.15	0.01	0.01	0.10	0.10	0.01	0.01	0.01	Bal.

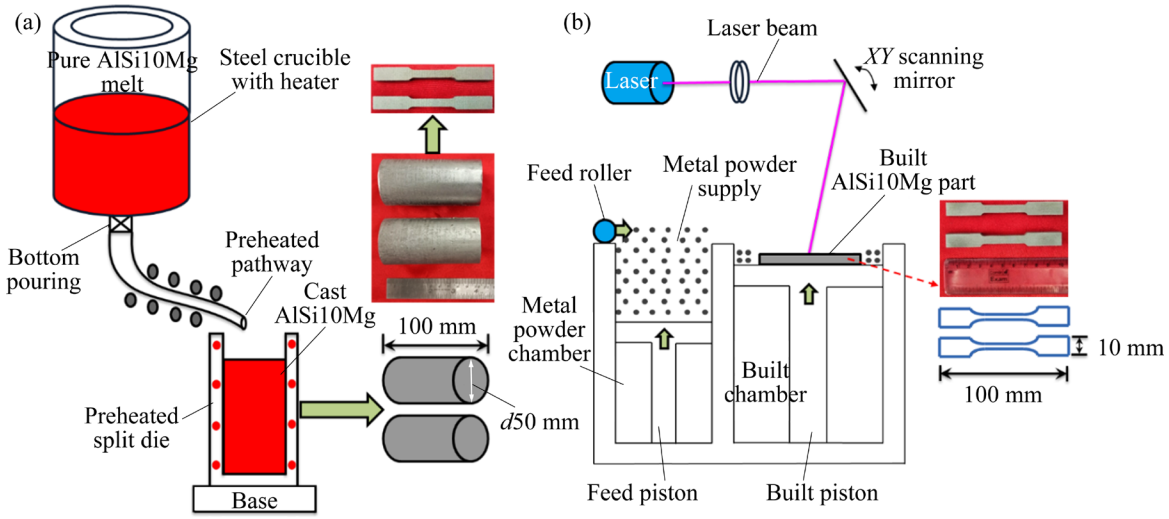

Fig. 1 Schematic diagrams representing (a) casting process and (b) SLM process along with tensile samples processed for further testing

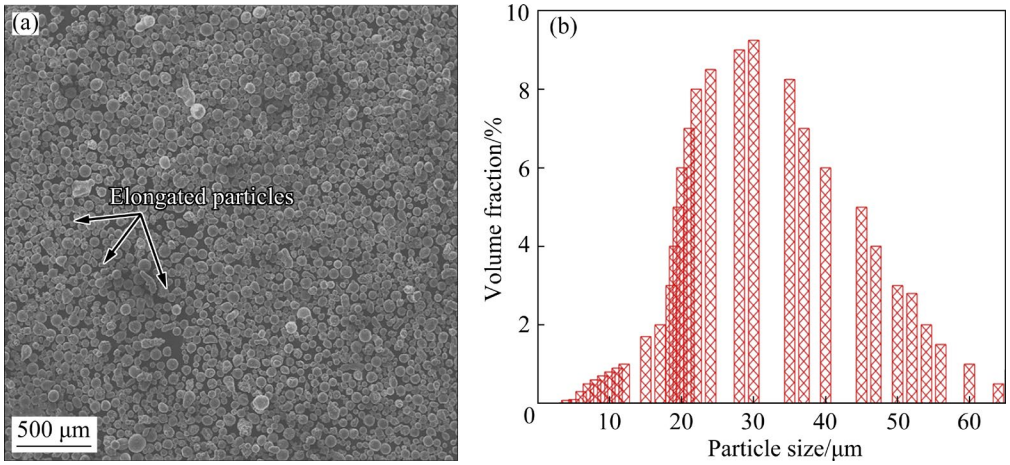

Fig. 2 (a) SEM powder surface morphology of recycled AlSi10Mg powder; (b) Graph representing particle size distribution

Table 2 Elemental constituents of AlSi10Mg powder utilized for producing SLM specimens (wt.%)

Condition	Si	Mg	Fe	Cu	Zn	Ti	Mn	Ni	Pb	Sn	Al
Standard (DIN-EN-1706)	9−11	0.2−0.45	<0.55	<0.05	<0.10	<0.15	<0.45	<0.05	<0.05	<0.05	Bal.
Measured	9.952	0.353	0.161	0.013	0.048	0.015	0.13	0.01	0.01	0.01	Bal.

Table 3 SLM process parameters used in this study to produce AlSi10Mg alloy

Laser power/W	Hatch spacing/mm	Laser scanning speed/(mm·s^{-1})	Layer thickness/mm	Orientation angle/(°)	Laser scanning strategy	Atmosphere
370	0.12	1300	0.03	67	Strip	Inert gas

AlSi10Mg samples, both as-produced and DA-treated, was analyzed using standard metallography methods as per ASTM E3-11, with Keller's reagent for etching. Investigations utilized both optical and SEM, integrated with an EBSD system to analyze the detailed microstructural features. A flat AlSi10Mg sample was electropolished in a solution of 80% methanol and 20% perchloric acid before EBSD analysis. Measurements were conducted with an FEI-FEG SEM equipped with an EBSD system, employing specific parameters: 60 nm step size, 70° tilting angle, and 20 kV acceleration voltage.

2.5 Assessment of tensile behaviour, work hardening rate, SEM and EBSD texture analysis on necked region of fractured surface

Tensile test samples (NHT-AC, DA-C, NHT-AB, and DA-B alloys) were prepared in accordance with ASTM E8 standards. Fishbone-shaped, with a total length of 100 mm and a gauge length of 32 mm, underwent room temperature tensile tests at a constant strain rate (1×10^{-4} s^{-1}) using an MTS universal tensile testing machine (UTM). During the tensile test, under each condition (NHT-AC, DA-C, NHT-AB and DA-B AlSi10Mg), three trails were taken and the average values were recorded. The observed results from the three trials were consistent with the minimal deviation indicating the good repeatability of the tensile test. In the post-tensile testing, fracture surfaces were analyzed via SEM, and the necked region underwent EBSD analysis. Work hardening rates during plastic deformation were calculated from true stress vs true strain values, with double logarithmic plots generated for NHT-AC, DA-C, NHT-AB, and DA-B alloys.

3 Results and discussion

3.1 Microstructure

Figures 3(a−d) illustrate the microstructural characteristics of NHT-AC, DA-C, NHT-AB, and DA-B alloys captured through SEM. Notably, the cast AlSi10Mg alloy displays a coarser Si eutectic phase (Figs. 3(a, b)), while the SLM-processed counterpart exhibits a cellular grain structure with

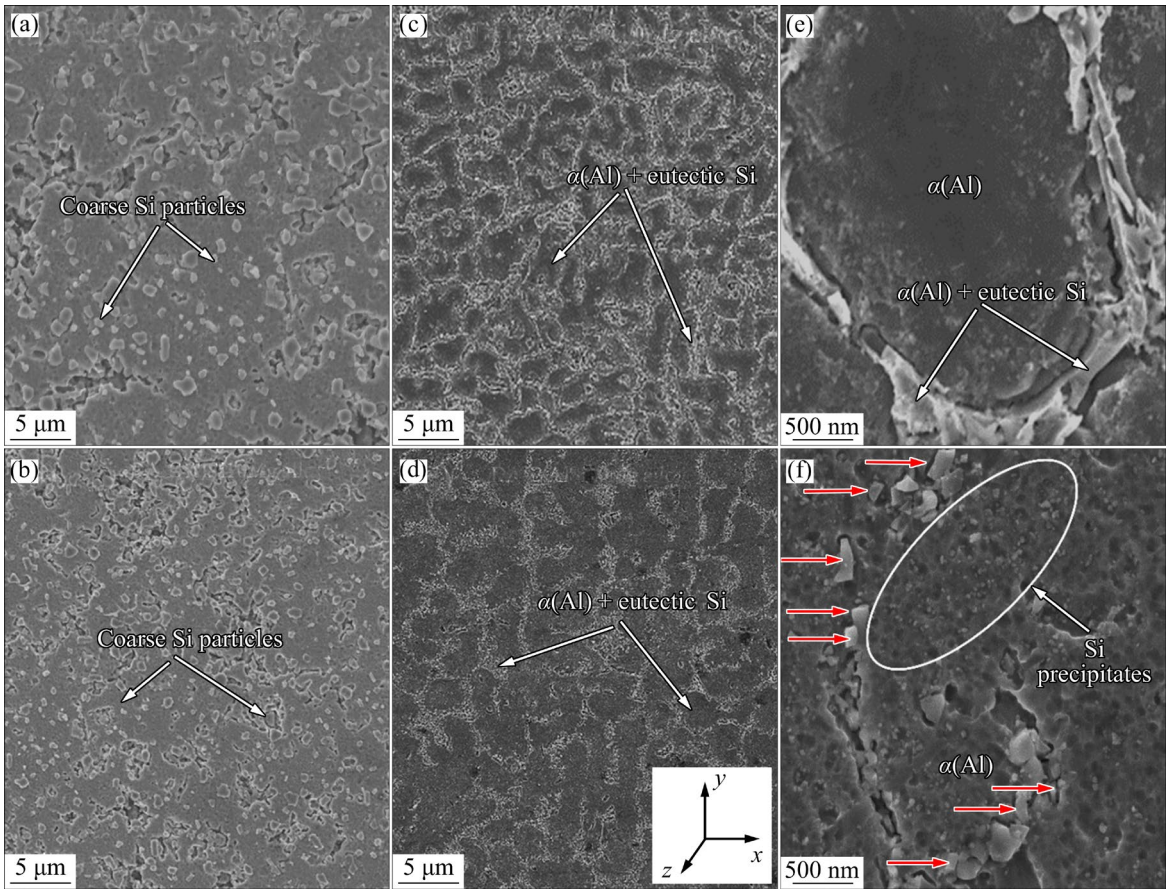

Fig. 3 SEM micrographs of (a) NHT-AC, (b) DA-C, (c) NHT-AB and (d) DA-B AlSi10Mg alloy captured in transverse direction; Magnified views of (e) NHT-AB alloy and (f) DA-B alloy (Red arrows: Fibrous rod-like Si particles)

α(Al) intertwined with a Si-enriched eutectic phase (Fig. 3(c)). The dissimilarities arise from distinct cooling rates and solidification conditions inherent in casting and SLM methods. Conventional casting (10^2 °C/s or less) has a slower cooling rate than SLM (10^3−10^6 °C/s), leading to a fine-grained cellular network structure in the SLM-produced NHT-AB alloy. This emphasizes the microstructural impact of fabrication techniques on AlSi10Mg alloy. In Fig. 3(d), the cellular microstructure with a fibrous Al/Si eutectic along cell boundaries persists through the DA thermal treatment, maintaining its integrity despite a not very low temperature. Furthermore, DA-B alloy exhibits Si nanoprecipitates within the cell boundary (Fig. 3(f)), contrasting with NHT-AB alloy (Fig. 3(e)). The DA heat treatment induces Si nano particle precipitation, enhancing the mechanical properties of the AlSi10Mg alloy. Additionally, the aspect ratio (AR) of fibrous Si in the cell boundary changes the shape. Typically, during SHT or T6 thermal treatment, fibrous eutectic Si particles undergo fragmentation, spheroidization (AR≈1), and coarsening through the Ostwald mechanism observed elsewhere [43,44], diminishing alloy properties. In this study, the AR of eutectic Si particles was qualitatively observed to be greater than one (Fig. 3(f)), limiting spheroidization to particle fragmentation (AR>1).

3.2 Crystal orientation

The Schmid factor distribution map and bar graphs from EBSD analysis of AlSi10Mg alloys are shown in Fig. 4. The Schmid factor, indicating microstructural attributes and deformability under stress, was crucial [45]. Higher Schmid factors imply increased susceptibility to slip activation [46], whereas lower values hinder dislocation movement [47], thereby enhancing mechanical performance. NHT-AC AlSi10Mg had the highest mean Schmid factor (0.4819), suggesting greater slip occurrence. Conversely, DA-C AlSi10Mg alloy (mean 0.4753) exhibited improved mechanical properties, although still higher than those of SLMed AlSi10Mg Alloy. NHT-AB and DA-B AlSi10Mg alloys (mean 0.4645)

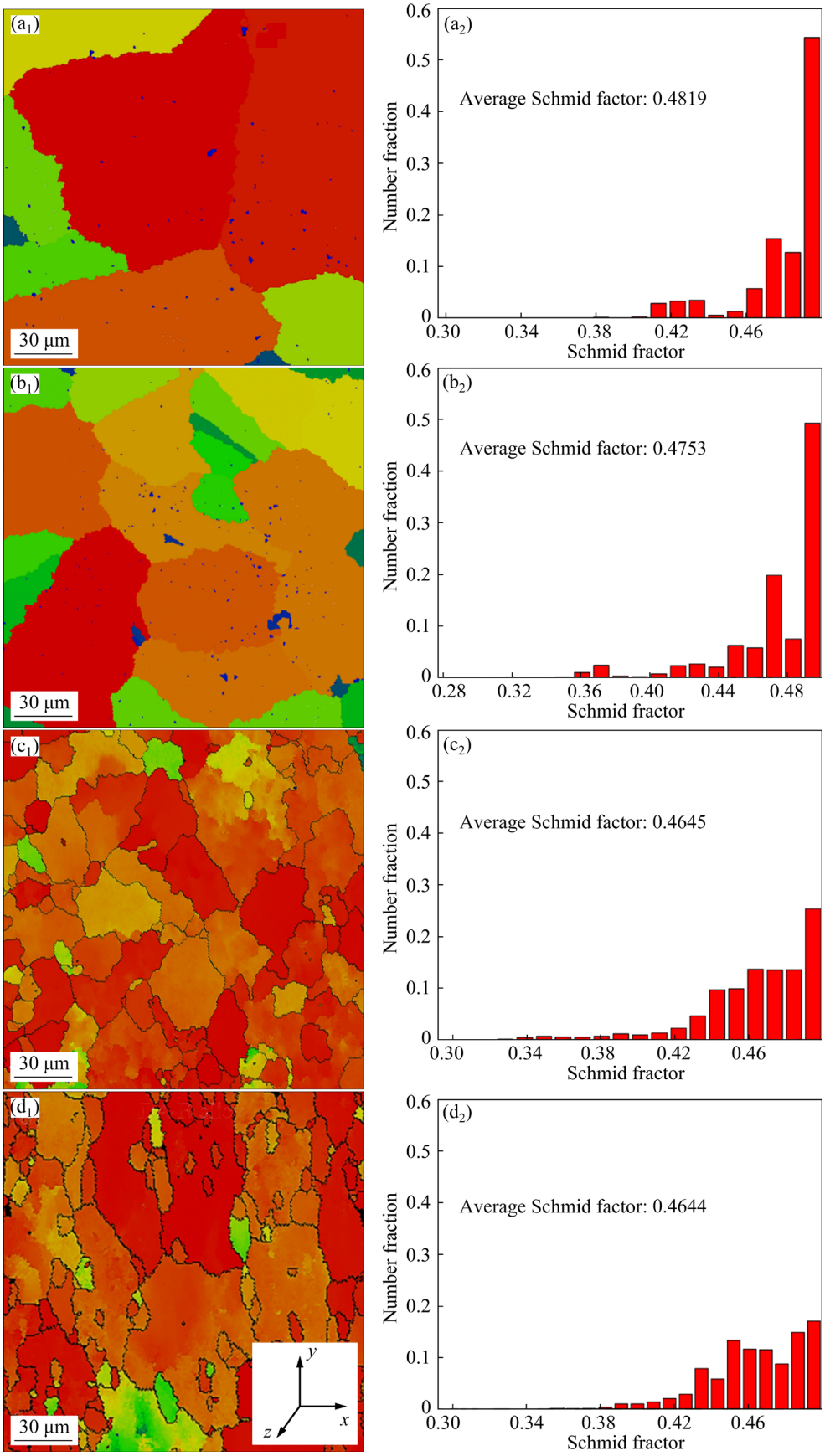

Fig. 4 Schmid factor distribution map (a_1−d_1) and histograms (a_2−d_2) extracted from EBSD analysis observed in transverse cross section of AlSi10Mg alloys: (a_1, a_2) NHT-AC; (b_1, b_2) DA-C; (c_1, c_2) NHT-AB; (d_1, d_2) DA-B

showed enhanced mechanical properties compared to the cast counterpart. Identical Schmid factor values in NHT-AB and DA-B were correlated with their similar microstructures. Overall, NHT-AC AlSi10Mg alloy was easier to deform due to greater dislocation movement, while SLMed AlSi10Mg alloy hindered dislocation movement, improving mechanical performance. The results align with the tensile test outcomes, indicating a correlation among Schmid factor, deformability, and mechanical properties in the AlSi10Mg alloys.

The effect of heat treatment conditions on the crystallographic texture orientations are further examined with the inverse pole figures (IPFs) extracted from the EBSD analyses. Figure 5 shows the IPFs obtained from EBSD analyses which depicts the transverse cross-section of AlSi10Mg alloy after different heat treatment processes. The overall texture intensity of the specimens was quantified in terms of the texture strength [48] (which is a square root of the texture index) as depicted in the Fig. 5. Here, all samples exhibited a texture strength of more than one indicating the anisotropic nature. This anisotropic nature was attributed to the rapid solidification process during manufacturing, which significantly affected the mechanical properties. These characteristics promote directional grain growth and preferred crystallographic orientations leading to improved strength and ductility along specific crystallographic directions due to alignment of slip planes. Heat treatment further alters the texture due to changes in the residual stress state promoting grain growth. For instance, the DA process improves the grain orientations which was expected to improve the mechanical stability and strength. Conversely,

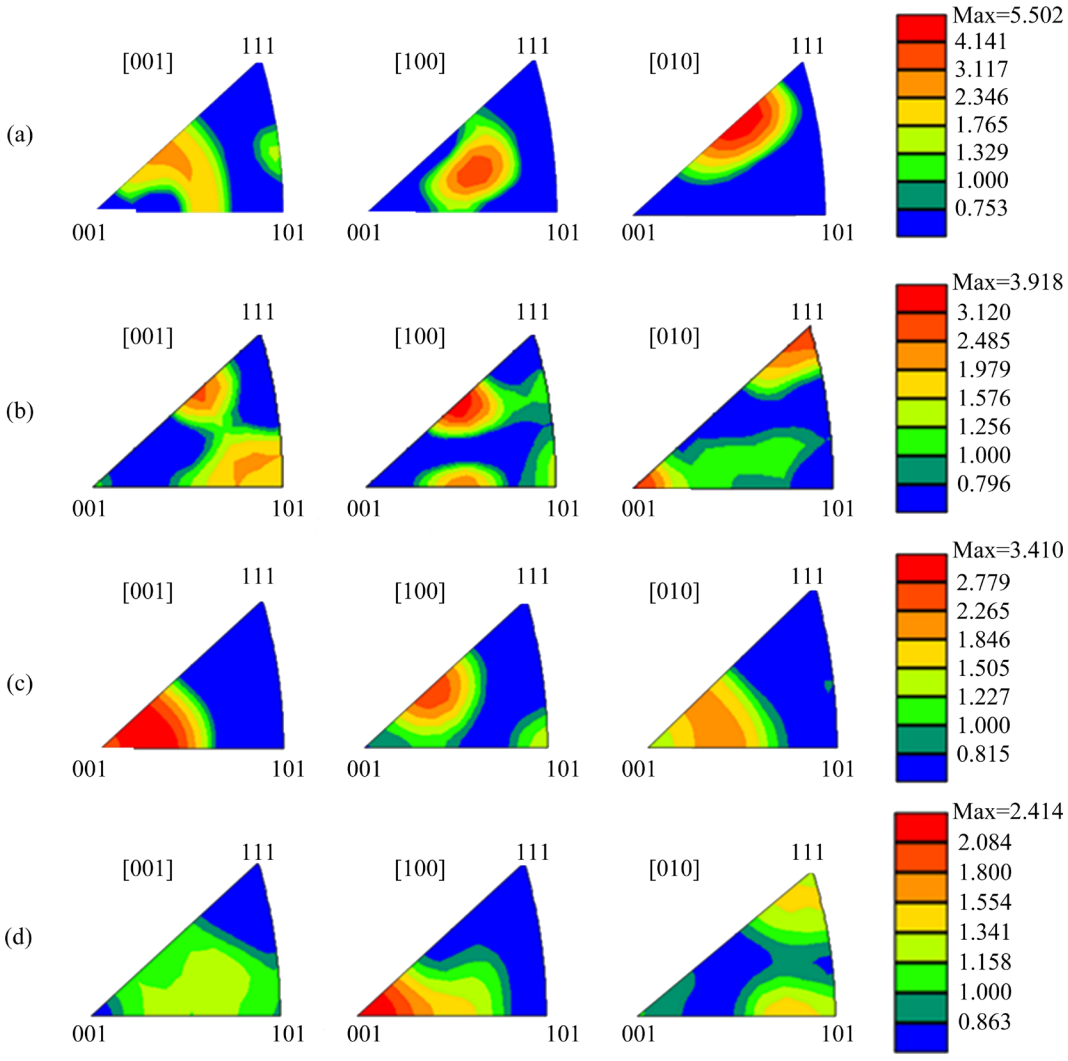

Fig. 5 Inverse pole figures extracted from EBSD analysis observed in transverse cross section of AlSi10Mg alloys: (a) NHT-AC; (b) DA-C; (c) NHT-AB; (d) DA-B

as-built (AB) samples were expected to retain a high degree of randomness in texture which reduces the anisotropy.

3.3 Tensile behavior

Figure 6 displays the engineering stress−strain plots of AlSi10Mg alloys under NHT-AC, DA-C, NHT-AB, and DA-B conditions, with corresponding tensile properties in Table 4. NHT-AC AlSi10Mg exhibits the lowest YS ((128.38±2) MPa) and UTS ((209.92±4) MPa), consistent with its high Schmid factor promoting slip occurrence. DA-C AlSi10Mg has a slight increase in YS ((136.65±2) MPa) and UTS ((212.34±6) MPa), aligning with the reduced average Schmid factor. However, both values remain lower than those of the SLM counterpart. The cast AlSi10Mg alloy, with larger grains (Fig. 4(a)) from slower cooling rates during casting, shows the lowest YS and UTS, further highlighting the impact of fabrication processes on mechanical properties. Overall, the tensile properties demonstrate the influence of microstructure, Schmid factor, and cooling rates on the mechanical behavior of AlSi10Mg alloys.

The SLM-produced AlSi10Mg alloy exhibits superior YS and UTS compared to its cast counterpart. NHT-AB alloy demonstrates an YS of (230.31±1) MPa and UTS of (373.10±3) MPa, significantly surpassing the cast alloy. YS and UTS of NHT-AB alloy are improved by 79.39% and 77.73%, respectively, over NHT-AC alloy. The enhanced tensile behavior in NHT-AB alloy is attributed to rapid cooling in the SLM process, leading to solid solution strengthening, a fine-grain structure, and the development of a eutectic cell structure, impeding dislocation movement. The average Schmid factor (0.4645, Fig. 4) for NHT-AB alloy indicates improved hindrance to dislocation motion during tensile loading, contributing to increased YS and UTS in the alloy.

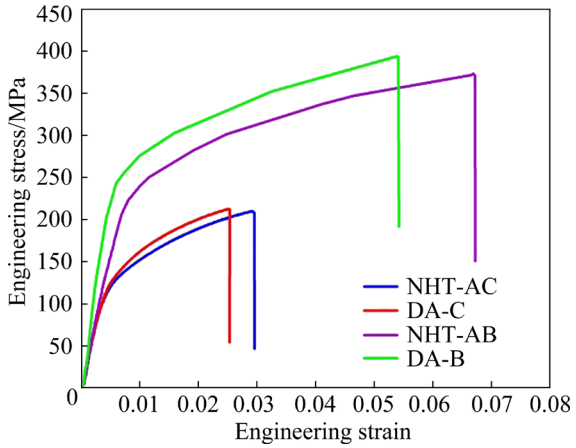

Fig. 6 Variation of engineering tensile stress−strain curves of AlSi10Mg alloys under different conditions (NHT-AC, DA-C, NHT-AB and DA-B)

The YS and UTS of SLM-produced AlSi10Mg alloy were further improved with the application of the DA heat treatment. DA-B AlSi10Mg alloy exhibited superior YS ((251.59±1) MPa) and UTS ((393.84±3) MPa) compared to other samples, marking a 95.97% increase in YS and an 87.61% increase in UTS over the NHT-AC alloy. In contrast to the NHT-AB alloy, DA-B showed a 9.24% increase in YS and a corresponding 5.56% enhancement in UTS. The strength improvement in DA-B AlSi10Mg is attributed to hard nano Si precipitates resisting deformation under tensile loading and an enhanced work hardening rate. Figure 7 compares UTS values from previous studies, highlighting that DA treatment strengthens the SLM-fabricated AlSi10Mg alloy, contrary to findings in many prior studies where post-heat treatment resulted in decreased UTS due to silicon particle isolation and growth from the cellular network [17,19,20,23,27,39,41,42].

The fracture strength of the DA-B AlSi10Mg alloy (191.54 MPa) surpassed that of NHT-AC (46.36 MPa), DA-C (54.11 MPa), and NHT-AB AlSi10Mg alloy (150.58 MPa). Additionally, the modulus of toughness (the area below the engineering stress−strain curve) and the modulus of

Table 4 Tensile properties of AlSi10Mg alloys under different conditions

Condition	YS/MPa	Strain at yield	UTS/MPa	Strain at ultimate point	Modulus of toughness/(J·mm^{-3})	Modulus of resilience/(J·mm^{-3})
NHT-AC	128.38±2	0.0059	209.92±4	0.029	4.67	0.46
DA-C	136.65±2	0.0063	212.34±6	0.025	3.99	0.51
NHT-AB	230.31±1	0.0089	373.10±3	0.067	19.71	1.18
DA-B	251.59±1	0.0069	393.84±3	0.054	16.98	1.03

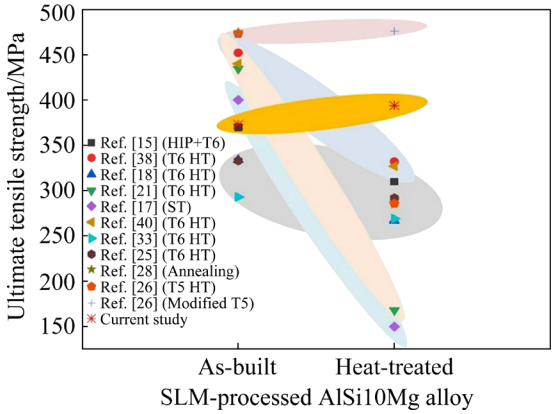

Fig. 7 Comparison of UTS reported in previous studies and current study

resilience (the area below the yield point) were improved in the DA-B AlSi10Mg alloy (Table 4), highlighting the effectiveness of DA heat treatment as a viable alternative for enhancing the properties of SLM-fabricated AlSi10Mg alloy.

3.4 Work hardening rate and strain hardening exponent

Experimental results allow for the calculation of the work hardening rate (WHR) during plastic deformation using Eq. (1) [47,49]. WHR, denoted by Θ, is determined by the successive variations in true stress ($\mathrm{d}\sigma_T$) and true strain rates ($\mathrm{d}\varepsilon_T$). A higher WHR signifies reduced stress-free homogeneous deformation, leading to the development of ribbon-like grains. Conversely, a lower WHR indicates elevated stress regions in grains, resulting in the appearance of pinch-off grains with equiaxed morphology [49].

$$\Theta = \mathrm{d}\sigma_T / \mathrm{d}\varepsilon_T \quad (1)$$

In Fig. 8, the change in WHR with respect to true strain is depicted for AlSi10Mg alloys under NHT-AC, DA-C, NHT-AB, and DA-B conditions. Two distinct WHR stages are observed. Initially, all test samples exhibit decreasing WHR with true strain, indicating strain softening and dislocation interaction. Subsequently, WHR is marginally improved, especially for NHT-AB and DA-B alloys, suggesting strain hardening. NHT-AC AlSi10Mg alloy shows lower WHR compared to the DA-C and SLM counterparts. Although DA-C AlSi10Mg alloy exhibits slightly higher WHR than NHT-AC, it remains lower than that of the SLM counterpart. Reduced strain hardening in the cast AlSi10Mg alloy, attributed to larger grains from slower cooling during casting, explains this phenomenon.

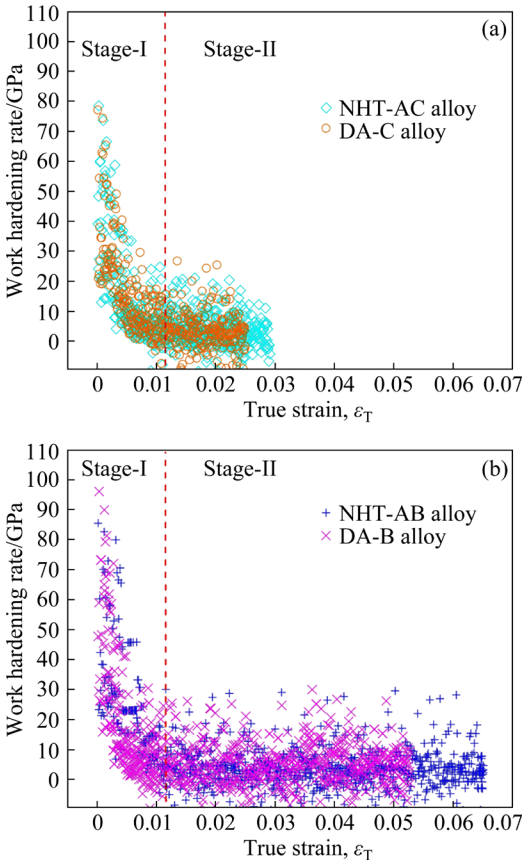

Fig. 8 Variation of WHR with respect to true strain of AlSi10Mg alloys under (a) NHT-AC and DA-C, and (b) NHT-AB and DA-B conditions

The WHR in the SLM-produced AlSi10Mg alloy is significantly higher than that in traditionally cast alloy, attributed to the faster cooling rate in SLM. NHT-AB and DA-B AlSi10Mg alloys, exhibit slightly higher WHR than the cast counterpart due to α(Al) strain hardening, eutectic cellular structure formation from solid solution strengthening, and higher-angle grain boundaries. Double logarithmic curves with true stress−true strain values for AlSi10Mg alloys under NHT-AC, DA-C, NHT-AB, and DA-B conditions are graphed in Fig. 9. The value of n in the Hollomon equation (Eq. (2)) is derived from these curves, representing the rapid rise of internal strength during loading in the alloy [50].

$$\sigma_T = K\varepsilon_T^n \quad (2)$$

where K is strength coefficient, and n is strain hardening exponent.

In the plastic region, the calculated n value was the highest for the DA-C AlSi10Mg alloy (0.2185),

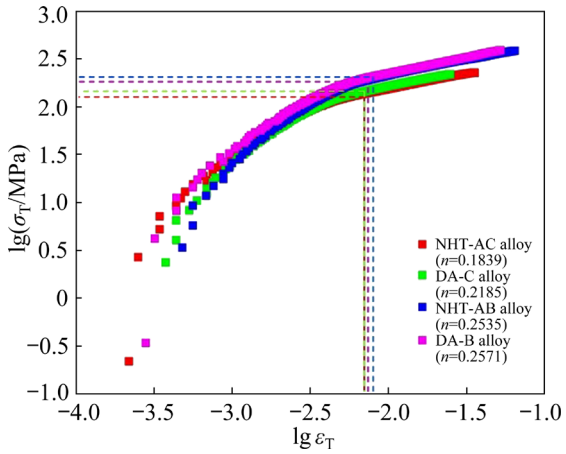

Fig. 9 Double logarithmic curves graphed with values of true stress−true strain curves for AlSi10Mg alloys under NHT-AC, DA-C, NHT-AB and DA-B conditions

surpassing that of the NHT-AC AlSi10Mg alloy (0.1839). Furthermore, *n* increased to 0.2535 for the NHT-AB alloy and 0.2571 for the DA-B alloy, signifying more pronounced plastic deformation and superior tensile behavior in the SLM-processed AlSi10Mg alloy. Eutectic Si ribbon formation, solid solution strengthening, and precipitated nano Si particles during the DA heat treatment contribute to this enhanced performance. Overall, compared to cast samples, SLM-processed AlSi10Mg alloy exhibits the maximum *n* value, indicating a rapid rise in internal strength during tensile loading.

3.5 Fracture surface morphology

The fracture surface analysis of tensile-tested samples reveals distinct characteristics. SEM images in Fig. 10 display the tortuous surface of the fractured NHT-AC AlSi10Mg alloy. In comparison, the fracture surfaces of SLM-produced AlSi10Mg alloys, represented by the NHT-AB and DA-B in Fig. 11, exhibit a relatively smoother surface, indicating differences in the fracture morphology between cast and SLM-produced samples. The fracture surfaces of the NHT-AC (Figs. 10(a, b)) and DA-C (Figs. 10(c, d)) AlSi10Mg alloys exhibit large dimples and cleavages, indicating a combination of ductile and brittle characteristics in the cast AlSi10Mg alloy. Dimples confirm ductile fracture,

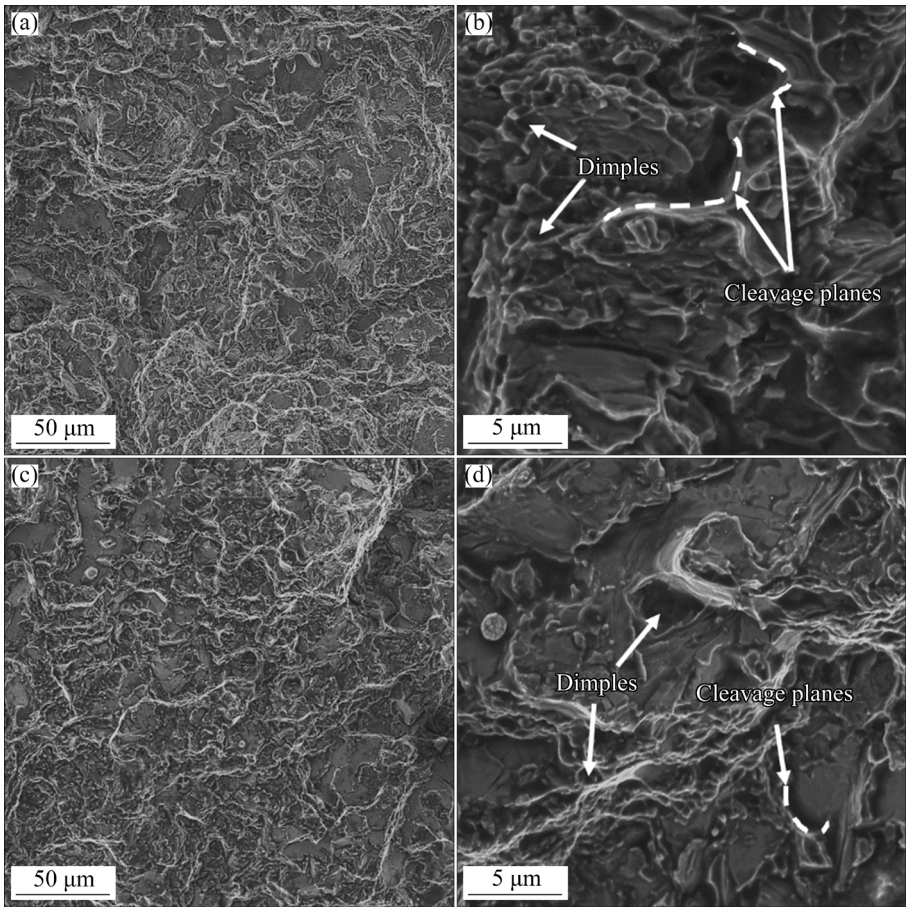

Fig. 10 SEM microstructures of tensile fractured surfaces of (a, b) NHT-AC and (c, d) DA-C AlSi10Mg alloys (The dashed lines indicate the cleavage planes)

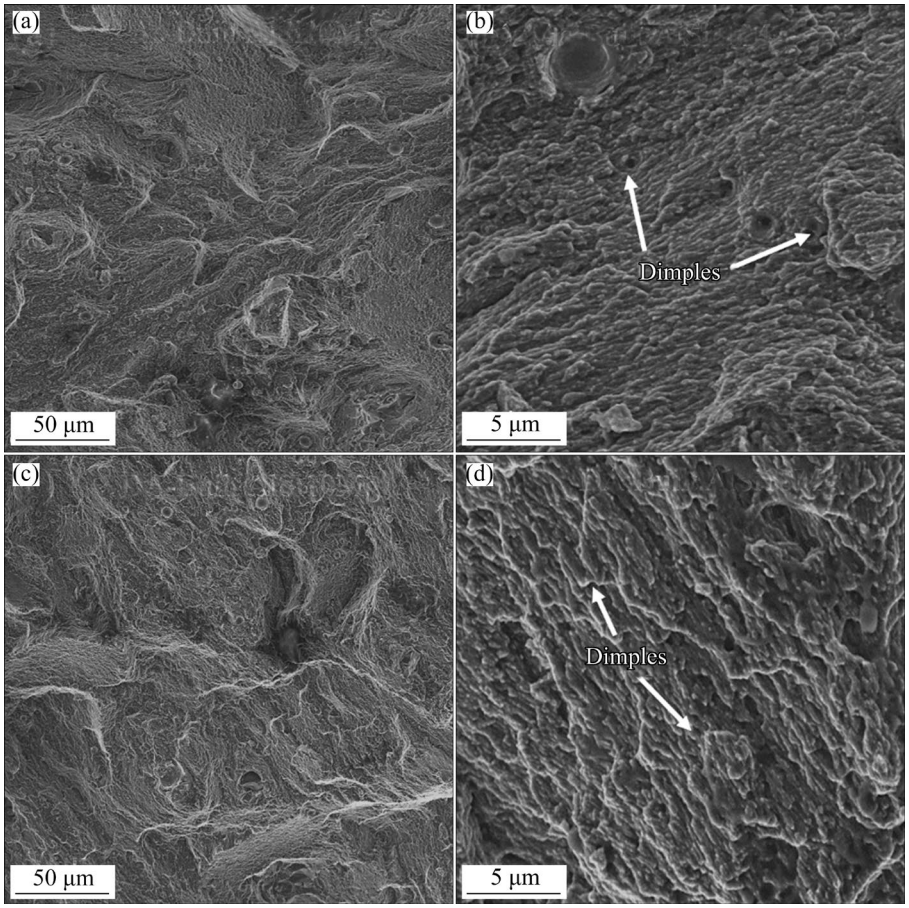

Fig. 11 SEM microstructures of tensile fractured surfaces of (a, b) NHT-AB and (c, d) DA-B AlSi10Mg alloys

while cleavages signify brittle fracture. Compared to the SLM-processed AlSi10Mg alloy, the fracture surface of cast alloy exhibits a relatively lower ductility, consistent with the explained variation in ductility through WHR, as presented in Fig. 8. In contrast to the cast AlSi10Mg alloy, the fracture surface morphology of the NHT-AB alloy (Figs. 11(a, b)) displays a smoother surface with fine dimples, indicating a ductile fracture mechanism. Similar observations were made with the DA-B alloy (Figs. 11(c, d)), where an increased quantity of dimples confirms a ductile fracture. Moreover, no signs of Si particle decohesion were observed in the fracture surfaces of both the NHT-AB AlSi10Mg and DA-B AlSi10Mg alloys, affirming a sound interfacial bonding between the α(Al) and eutectic Si phases.

3.6 Texture analysis

To assess the sample deformation after the tensile test, it is crucial to study the EBSD microstructural characteristics observed in the necked region of the tensile fractured surface. Figure 12 displays the EBSD coloured IPF map and misorientation angle distribution chart of the NHT-AC, DA-C, NHT-AB and DA-B alloys. The results of NHT-AC (Figs. 12(a_1, a_2)) reveal coarser and deformed grains with shifted grain boundary misorientation angles, particularly toward high-angle grain boundaries (HAGBs). The slow cooling rate during fabrication led to coarse grains in NHT-AC, resulting in increased plastic deformation (Fig. 6) and strength after the tensile test. The shift toward HAGBs after the tensile test indicates a structural response to the deformation. Similar analyses were conducted on the other samples (DA-C, NHT-AB, and DA-B) to comprehensively understand their microstructural changes after the tensile testing. Grain boundary misorientation angles between 0° and 15° were identified as low-angle grain boundaries (LAGBs), while those between 15° and 65° were classified as HAGBs. In the NHT-AC alloy, the distribution of misorientation angles, particularly HAGBs, slightly increased after tensile deformation (Fig. 12(a_2)). The deformation-related changes were also observed in DA-C AlSi10Mg

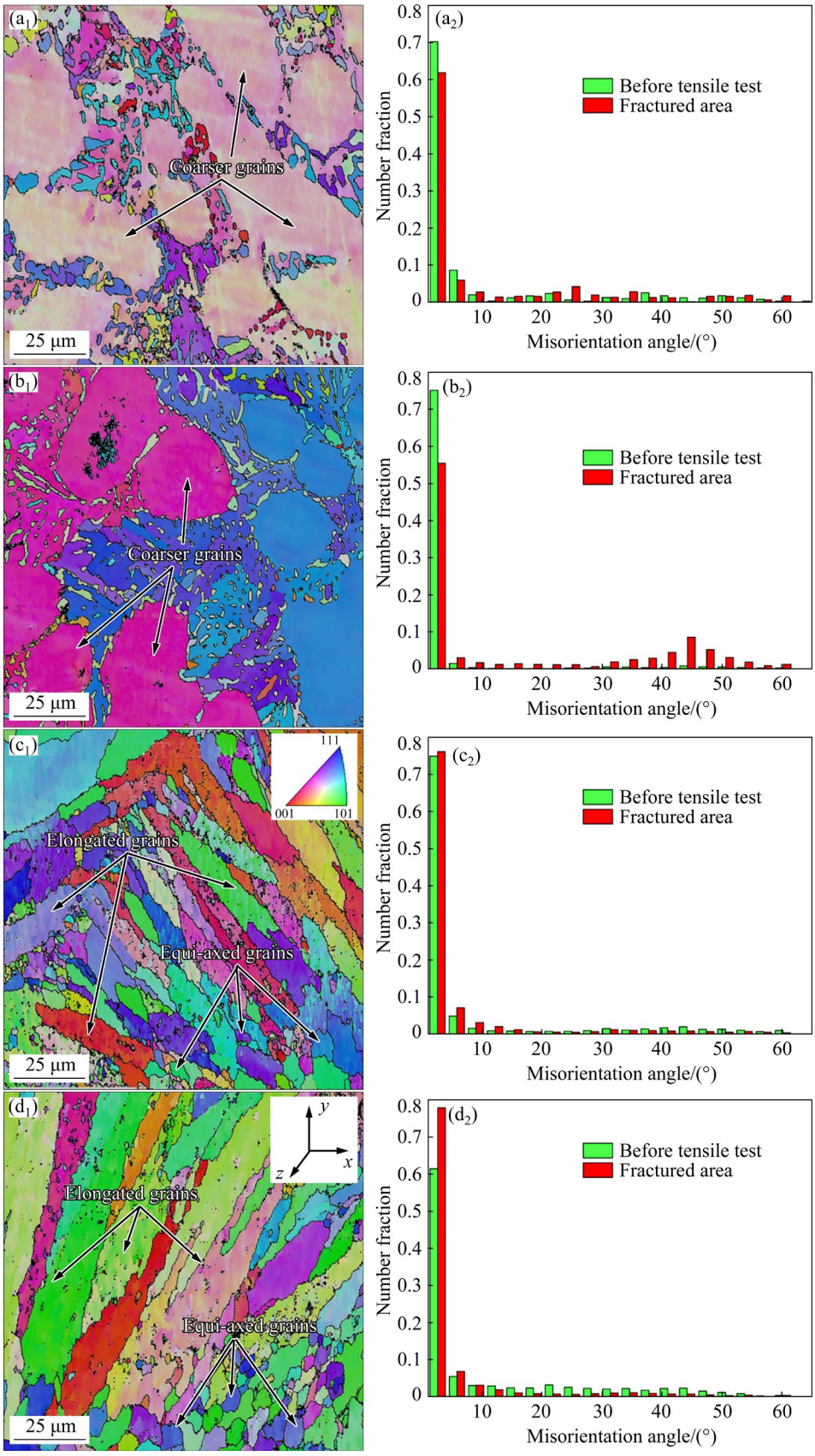

Fig. 12 EBSD analysis observed in necked region of tensile fractured sample under (a_1, a_2) NHT-AC, (b_1, b_2) DA-C, (c_1, c_2) NHT-AB, and (d_1, d_2) DA-B conditions captured in transverse direction: (a_1−d_1) EBSD coloured IPF map; (a_2−d_2) Misorientation angle distribution

alloy (Fig. 12(b_1)), showing misorientation angle distributions along LAGBs and HAGBs (Fig. 12(b_2)). The distinct grain sizes in cast and SLM-processed AlSi10Mg alloys were evident in the EBSD analysis of deformed tensile samples (Figs. 12(c_1, d_2)). In Fig. 12(c_1, c_2), the EBSD analysis of the NHT-AB alloy reveals a transition from equiaxed to elongated high-aspect-ratio grains in the necked region after tensile deformation. The Misorientation angle distribution chart (Fig. 12(c_2)) demonstrates a substantial increase (88.45%) in LAGBs, indicating the formation of subgrain structures due to dislocation rearrangement and dynamic recovery. SEM micrographs extracted from the EBSD analysis (Fig. 13) visually confirm the deformation process. Similarly, for the DA-B alloy, elongated grains (Fig. 12(d_1)) and a significant increase (89.62%) in LAGBs were observed (Fig. 12(d_2)). This evolution of LAGBs and sub-grains in the DA-B alloy contributes to enhanced material strength through the Hall−Petch effect, reinforcing the mechanical properties of the alloy [51].

3.7 Strengthening mechanisms of AlSi10Mg alloy

The strength of the AlSi10Mg alloy, whether cast or produced through SLM, can be theoretically explained by considering three key strengthening mechanisms [16]: (1) cell boundary or Hall−Petch strengthening [15], (2) precipitation or Orowan strengthening [16], and (3) solid solution strengthening [15]. The enhanced strength of the SLM-produced alloy is primarily attributed to these mechanisms. Considering the strengthening mechanisms, the strength of the AlSi10Mg alloy can be estimated using Eq. (3), where σ_0 represents the internal friction stress [16]. The parameters necessary for calculating the strengthening mechanisms of the AlSi10Mg alloy are provided in Table 5.

$$\sigma_y=\sigma_0+\sigma_{HP}+\sigma_{OR}+\sigma_{SS} \tag{3}$$

Cell boundary strengthening (σ_{HP}), resulting from the cellular network formed during the SLM process, is calculated using Eq. (4), where k is a material constant [15] and d is the cell diameter.

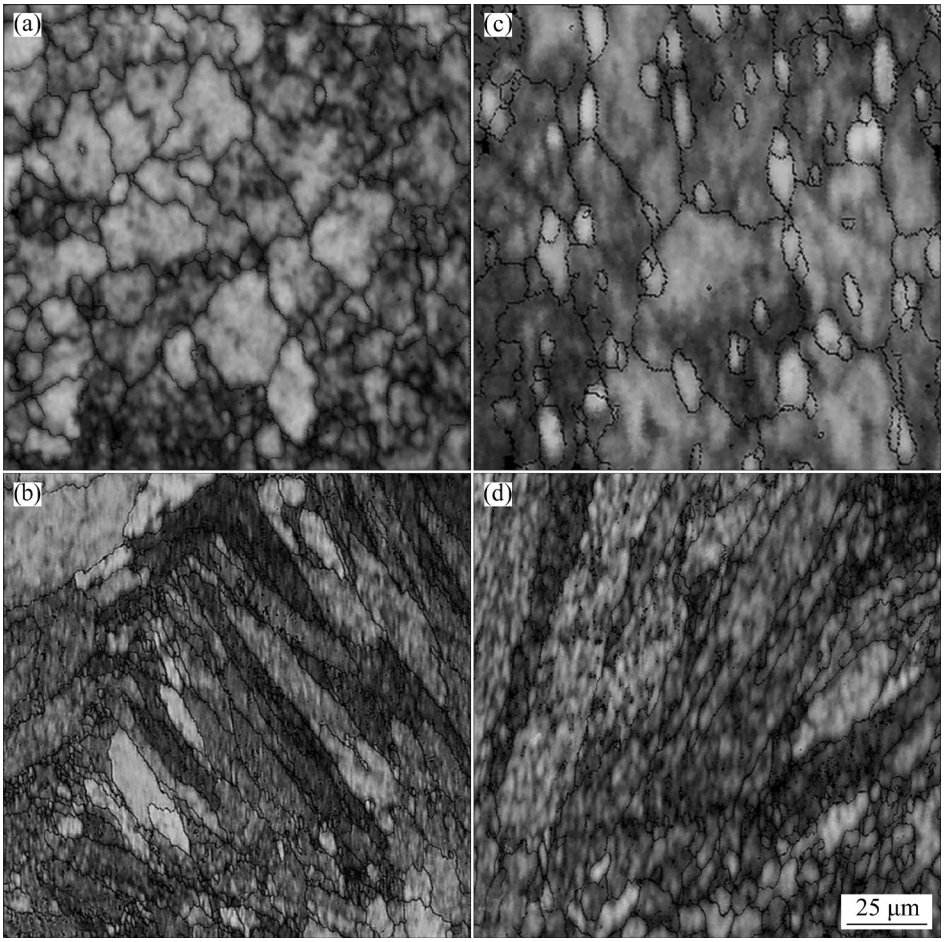

Fig. 13 SEM micrographs of (a, b) NHT-AB alloy and (c, d) DA-B alloy extracted (a, c) before and (b, d) after tensile test on necked region of tensile fractured sample

Table 5 Strengthening mechanism parameters used in theoretical calculation of YS

Parameter	Value	Source
Internal friction stress, σ_0/MPa	72	Ref. [16]
Material constant, k/(MPa·m$^{1/2}$)	~0.06	Ref. [15]
Cell diameter, d/μm	210 (NHT-AC), 165 (DA-C), 2.10 (NHT-AB), 1.99 (DA-B)	Current study
Material constant, φ	0.4	Ref. [16]
Shear modulus of Al matrix, G/GPa	26.5	Ref. [16]
Burgers vector of Al, b/nm	0.286	Ref. [16]
Diameter of Si precipitates, d_{Si}/nm	23.5 (NHT-AC), 21.6 (DA-C), 11.6 (NHT-AB), 10.1 (DA-B)	Current study
Volume fraction of Si precipitates, v_{Si}/%	2.5	Ref. [16]
Scaling factor for Si element, k_{Si}/(MPa·wt.%$^{-1}$)	11	Ref. [15]
Scaling factor for Mg element, k_{Mg}/(MPa·wt.%$^{-1}$)	17	Ref. [15]
Exponential factor, m	1	Ref. [15]
Solid solution content of Si, C_{Si}/wt.%	0.10 (NHT-AC), 0.15 (DA-C), 1.00 (NHT-AB), 0.70 (DA-B)	Current study
Solid solution content of Mg, C_{Mg}/wt.%	0.206 (NHT-AC), 0.210 (DA-C), 0.204 (NHT-AB), 0.200 (DA-B)	Current study

The microstructural analysis (Fig. 3(b)) reveals the presence of a cellular network with eutectic Si in the SLM-processed AlSi10Mg alloy, contributing to its cell boundary strengthening.

$$\sigma_{HP}=k/\sqrt{d} \tag{4}$$

Considering the cell diameter in Eq. (4), σ_{HP} was calculated as 4.14 MPa (NHT-AC AlSi10Mg alloy), 4.67 MPa (DA-C AlSi10Mg alloy), 41.37 MPa (NHT-AB AlSi10Mg alloy), and 42.58 MPa (DA-B AlSi10Mg alloy). The differences in microstructural features between cast and SLM processed AlSi10Mg alloys were evident in the reduced cellular boundary strengthening for both the NHT-AC and DA-C alloys. The decreased cellular boundary strengthening in the cast AlSi10Mg alloy corresponds to the slower cooling rate in the casting process, resulting in samples with coarse grains. Notably, the calculated values of cell boundary strength were identical for both the NHT-AB and DA-B alloy, attributed to the uniform cell structure size observed in NHT-AB and DA-B alloy.

σ_{OR} represents the precipitation or Orowan strengthening mechanism resulting from the Si precipitates during fabrication. σ_{OR} was calculated using Eq. (5), where φ is the material constant, G is the shear modulus of the Al matrix, b is the magnitude of Burgers vector, d_{Si} is the diameter of Si precipitates, and v_{Si} is the volume fraction of Si precipitates. Values of σ_{OR} were 46.8 MPa (NHT-AC AlSi10Mg alloy), 50.99 MPa (DA-C alloy), 94.55 MPa (NHT-AB alloy), and 108.63 MPa (DA-B alloy). Enhanced strength in DA-B alloy was attributed to nano-sized Si precipitates within the cell boundary.

$$\sigma_{OR}=\frac{\varphi G b}{d_{Si}}\left(\frac{6v_{Si}}{\pi}\right)^{1/3} \tag{5}$$

σ_{ss} denotes solid solution strengthening, resulting from Si solubility in the Al matrix and is calculated using Eq. (6). The k_{Si} value in Eq. (6) refers to the scaling factor for the Si element, k_{Mg} refers to the scaling factor for the Mg element, C_{Si} is the solid solution content of Si, C_{Mg} is the solid solution content of Mg, and m is the exponential factor. With values of σ_{SS} at 4.50 MPa (NHT-AC), 5.05 MPa (DA-C), 14.4 MPa (NHT-AB), and 11.1 MPa (DA-B), the decrease in solid solution strengthening of DA-B AlSi10Mg alloy indicates reduced Si solubility, suggesting increased nano-sized Si precipitates due to DA heat treatment. Table 6 summarizes the influence of different

Table 6 Contribution of various strengthening mechanisms to improvement of mechanical properties of NHT-AC, DA-C, NHT-AB and DA-B AlSi10Mg alloy

Sample	σ_{HP}/MPa	σ_{OR}/MPa	σ_{SS}/MPa	Calculated YS/MPa	Measured YS/MPa	Error/%
NHT-AC	4.14	46.8	4.5	127.44	128.38	0.73
DA-C	4.67	50.99	5.05	132.71	136.65	2.88
NHT-AB	41.37	94.55	14.4	222.32	230.31	3.47
DA-B	42.58	108.63	11.1	234.31	251.59	6.87

strengthening mechanisms on overall strength enhancement in NHT-AC, DA-C, NHT-AB, and DA-B alloys, emphasizing the significant contribution of the precipitation or Orowan strengthening to the enhanced strength of the alloy followed by the cell boundary or Hall−Petch strengthening mechanism.

$$\sigma_{SS}=[k_{Mg}(C_{Mg})^m+k_{Si}(C_{Si})^m] \quad (6)$$

4 Conclusions

(1) Microstructural analysis revealed that the cast alloy exhibited a coarse Si eutectic phase, while the SLM alloy showed a fine-grained cellular structure with an intertwined α(Al) matrix and Si-enriched eutectic phase.

(2) The DA-B AlSi10Mg alloy demonstrated superior mechanical properties, including a 9.24% increase in YS and a 5.56% increase in UTS over the NHT-AB AlSi10Mg alloy and substantial improvement over the cast counterpart.

(3) Fracture surface analysis revealed a ductile fracture mechanism in the SLM alloys, with fine dimples observed, while the cast alloys displayed larger dimples and cleavages, indicating a combination of ductile and brittle fracture behavior.

(4) EBSD texture analysis revealed a transition from fine equiaxed grains to elongated high-aspect-ratio grains in the necked region after tensile deformation.

(5) Strengthening mechanisms highlighted the significant contribution from the precipitation or Orowan strengthening mechanism to the enhanced strength of the SLM alloys followed by the cell boundary or Hall−Petch strengthening. However, the cast alloys relied mainly on the precipitation or Orowan strengthening mechanism.

CRediT authorship contribution statement

A. SATHISHKUMAR: Formal analysis, Validation, Writing − Original draft; **R. SOUNDARARAJAN:** Visualization, Investigation, Data curation, Resources, Project administration; **S. SIVASANKARAN:** Conceptualization, Methodology, Investigation, Writing − Review & editing; **A. RAMESH:** Resources, Funding acquisition, Project administration.

Declaration of competing interest

The authors declare that they have no known competing financial interests or personal relationships that could have appeared to influence the work reported in this paper.

Ethics Approval Statement

All the authors have declared under their ethical and legal responsibility that the submitted paper is original and has not been submitted to the peer review process to any other journal. Also, all the authors have declared that the manuscript does not report or involve the use of any animal or human data or tissue.

References

[1] ASGARI H, BAXTER C, HOSSEINKHANI K, MOHAMMADI M. On microstructure and mechanical properties of additively manufactured AlSi10Mg_200C using recycled powder [J]. Materials Science and Engineering A, 2017, 707: 148−158.

[2] ROTH C C, TANCOGNE-DEJEAN T, MOHR D. Plasticity and fracture of cast and SLM AlSi10Mg: High-throughput testing and modeling [J]. Additive Manufacturing, 2021, 43: 101998.

[3] GOVIL K, KUMAR V, PANDEY D P, PRANEETH R, SHARMA A. Additive manufacturing and 3D printing: A perspective [C]//Advances in Engineering Design: Select Proceedings of FLAME 2018. Singapore: Springer, 2019: 321−334.

[4] MAGISETTY R, CHEEKURAMELLI N S. Additive manufacturing technology empowered complex electromechanical energy conversion devices and transformers [J]. Applied Materials Today, 2019, 14: 35−50.

[5] PESODE P, BARVE S. Additive manufacturing of metallic biomaterials: Sustainability aspect, opportunity, and challenges [J]. Journal of Industrial and Production Engineering, 2023, 40(6): 464−505.

[6] YOUSSEF H, EL-HOFY H, AHMED M. Fundamentals of additive manufacturing: Principles, technologies, and applications [M]. CRC Press, 2024.

[7] KHAN I, BARSOUM I, ABAS M, AL RASHID A, KOÇ M, TARIQ M. A review of extrusion-based additive manufacturing of multi-materials-based polymeric laminated structures [J]. Composite Structures, 2024: 118490.

[8] PRABU G, JEYAPRAKASH N, YANG C H, SIVASANKARAN S. Synergetic effect of piled-up material around the nanoindentation cavity on additively manufactured Cu−Cr−Zr alloy [J]. Materials Today Communications, 2023, 107691.

[9] JEYAPRAKASH N, KUMAR M S, YANG C-H, CHENG Y, RADHIKA N, SIVASANKARAN S. Effect of micro-structural evolution during melt pool formation on nano-mechanical properties in LPBF based SS316L parts [J]. Journal of Alloys and Compounds, 2024, 972: 172745.

[10] PAUL M J, LIU Q, BEST J P, LI X, KRUZIC J J, RAMAMURTY U, GLUDOVATZ B. Fracture resistance of AlSi10Mg fabricated by laser powder bed fusion [J]. Acta Materialia, 2021, 211: 116869.

[11] LI Y, GU D, ZHANG H, XI L. Effect of trace addition of ceramic on microstructure development and mechanical properties of selective laser melted AlSi10Mg alloy [J]. Chinese Journal of Mechanical Engineering, 2020, 33: 33.

[12] RIENER K, ALBRECHT N, ZIEGELMEIER S, RAMAKRISHNAN R, HAFERKAMP L, SPIERINGS A B, LEICHTFRIED G J. Influence of particle size distribution and morphology on the properties of the powder feedstock as well as of AlSi10Mg parts produced by laser powder bed fusion (LPBF) [J]. Additive Manufacturing, 2020, 34: 101286.

[13] CAO Y, LIN X, WANG Q Z, SHI S Q, MA L, KANG N, HUANG W D. Microstructure evolution and mechanical properties at high temperature of selective laser melted AlSi10Mg [J]. Journal of Materials Science & Technology, 2021, 62: 162−172.

[14] PARK T H, BAEK M S, HYER H, SOHN Y, LEE K A. Effect of direct aging on the microstructure and tensile properties of AlSi10Mg alloy manufactured by selective laser melting process [J]. Materials Characterization, 2021, 176: 111113.

[15] GHIO E, CERRI E. Additive manufacturing of AlSi10Mg and Ti6Al4V lightweight alloys via laser powder bed fusion: A review of heat treatments effects [J]. Materials, 2022, 15: 2047.

[16] HADAHZADEH A, BAXTER C, AMIRKHIZ B S, MOHAMMADI M. Strengthening mechanisms in direct metal laser sintered AlSi10Mg: Comparison between virgin and recycled powders [J]. Additive Manufacturing, 2018, 23: 108−120.

[17] TRADOWSKY U, WHITE J, WARD R M, READ N, REIMERS W, ATTALLAH M M. Selective laser melting of AlSi10Mg: Influence of post-processing on the microstructural and tensile properties development [J]. Materials & Design, 2016, 105: 212−222.

[18] ZHOU L, MEHTA A, SCHULZ E, McWILLIAMS B, CHO K, SOHN Y. Microstructure, precipitates and hardness of selectively laser melted AlSi10Mg alloy before and after heat treatment [J]. Materials Characterization, 2018, 143: 5−17.

[19] HAN Q, JIAO Y. Effect of heat treatment and laser surface remelting on AlSi10Mg alloy fabricated by selective laser melting [J]. The International Journal of Advanced Manufacturing Technology, 2019, 102: 3315−3324.

[20] WANG L F, SUN J, YU X L, SHI Y, ZHU X G, CHENG L Y, LIANG H H, YAN B, GUO L J. Enhancement in mechanical properties of selectively laser-melted AlSi10Mg aluminum alloys by T6-like heat treatment [J]. Materials Science and Engineering A, 2018, 734: 299−310.

[21] CHEN K J, HUNG F Y, LUI T S, TSAI C L. Improving the applicability of wear-resistant Al−10Si−0.5 Mg alloy obtained through selective laser melting with T6 treatment in high-temperature, and high-wear environments [J]. Journal of Materials Research and Technology, 2020, 9: 9242−9252.

[22] ZHANG C, ZHU H, LIAO H, CHENG Y, HU Z, ZENG X. Effect of heat treatments on fatigue property of selective laser melting AlSi10Mg [J]. International Journal of Fatigue, 2018, 116: 513−522.

[23] LI W, LI S, LIU J, ZHANG A, ZHOU Y, WEI Q, YAN C, SHI Y. Effect of heat treatment on AlSi10Mg alloy fabricated by selective laser melting: Microstructure evolution, mechanical properties and fracture mechanism [J]. Materials Science and Engineering A, 2016, 663: 116−125.

[24] ITURRIOZ A, GIL E, PETITE M M, GARCIANDIA F, MANCISIDOR A M, SAN SEBASTIAN M. Selective laser melting of AlSi10Mg alloy: influence of heat treatment condition on mechanical properties and microstructure [J]. Welding in the World, 2018, 62: 885−892.

[25] ALHAMMADI A, AL-KETAN O, KHAN K A, ALI M, ROWSHAN R, AL-RUB R K A. Microstructural characterization and thermomechanical behavior of additively manufactured AlSi10Mg sheet cellular materials [J]. Materials Science and Engineering A, 2020, 791: 139714.

[26] PADOVANO E, BADINI C, PANTARELLI A, GILI F, D'AIUTO F. A comparative study of the effects of thermal treatments on AlSi10Mg produced by laser powder bed fusion [J]. Journal of Alloys and Compounds, 2020, 831: 154822.

[27] ABOULKHAIR N T, MASKERY I, TUCK C, ASHCROFT I, EVERITT N M. The microstructure and mechanical properties of selectively laser melted AlSi10Mg: The effect of a conventional T6-like heat treatment [J]. Materials Science and Engineering A, 2016, 667: 139−146.

[28] ROSENTHAL I, SHNECK R, STERN A. Heat treatment effect on the mechanical properties and fracture mechanism in AlSi10Mg fabricated by additive manufacturing selective laser melting process [J]. Materials Science and Engineering A, 2018, 729: 310−322.

[29] TONELLI L, LIVERANI E, MORRI A, CESCHINI L. Role of direct aging and solution treatment on hardness, microstructure and residual stress of the A357 (AlSi7Mg0.6) alloy produced by powder bed fusion [J]. Metallurgical and Materials Transactions B, 2021, 52: 2484−2496.

[30] TAKATA N, KODAIRA H, SEKIZAWA K, SUZUKI A, KOBASHI M. Change in microstructure of selectively laser melted AlSi10Mg alloy with heat treatments [J]. Materials Science and Engineering A, 2017, 704: 218−228.

[31] ZHAO L, MACÍAS J G S, DING L, IDRISSI H, SIMAR A. Damage mechanisms in selective laser melted AlSi10Mg under as built and different post-treatment conditions [J]. Materials Science and Engineering A, 2019, 764: 138210.

[32] SHAKIL S I, HADADZADEH A, AMIRKHIZ B S, PIRGAZI H, MOHAMMADI M, HAGSHENAS M. Additive manufactured versus cast AlSi10Mg alloy: Microstructure and micromechanics [J]. Results in Materials, 2021, 10: 100178.

[33] CHEN B, MOON S K, YAO X, BI G, SHEN J, UMEDA J, KONDOH K. Strength and strain hardening of a selective laser melted AlSi10Mg alloy [J]. Scripta Materialia, 2017, 141: 45−49.

[34] MACONACHIE T, LEARY M, ZHANG J, MEDVEDEV A, SARKER A, RUAN D, LU G, FARUQUE O, BRANDT M. Effect of build orientation on the quasi-static and dynamic response of SLM AlSi10Mg [J]. Materials Science and Engineering A, 2020, 788: 139445.

[35] READ N, WANG W, ESSA K, ATTALLAH M M. Selective laser melting of AlSi10Mg alloy: Process optimisation and mechanical properties development [J]. Materials & Design, 2015, 65: 417−424.

[36] UZAN N E, SHNECK R, YEHESKEL O, FRAGE N. High-temperature mechanical properties of AlSi10Mg specimens fabricated by additive manufacturing using selective laser melting technologies (AM-SLM) [J]. Additive Manufacturing, 2018, 24: 257−263.

[37] YAN Q, SONG B, SHI Y. Comparative study of performance comparison of AlSi10Mg alloy prepared by selective laser melting and casting [J]. Journal of Materials Science & Technology, 2020, 41: 199−208.

[38] UZAN N E, SHNECK R, YEHESKEL O, FRAGE N. Fatigue of AlSi10Mg specimens fabricated by additive manufacturing

selective laser melting (AM-SLM) [J]. Materials Science and Engineering A, 2017, 704: 229−237.
[39] GIRELLI L, TOCCI M, GELFI M, POLA A. Study of heat treatment parameters for additively manufactured AlSi10Mg in comparison with corresponding cast alloy [J]. Materials Science and Engineering A, 2019, 739: 317−328.
[40] SURYAWANSHI J, PRASHANTH K G, SCUDINO S, ECKERT J, PRAKASH O, RAMAMURTY U. Simultaneous enhancements of strength and toughness in an Al−12Si alloy synthesized using selective laser melting [J]. Acta Materialia, 2016, 115: 285−294.
[41] SCHUCH M, HAHN T, BLECKMANN M. The mechanical behavior and microstructure of additively manufactured AlSi10Mg for different material states and loading conditions [J]. Materials Science and Engineering A, 2021, 813: 141134.
[42] SATHISHKUMAR A, SOUNDARARAJAN R, SIVASANKARAN S, RAMESH A. Influence of eutectic-Si in as-cast and fibrous-eutectic-Si in LPBF-processed AlSi10Mg alloys on wear and corrosion behaviors treated with direct aging route [J]. Journal of Materials Science, 2023, 58: 14889−14910.
[43] ALGHAMDI F, SONG X, HADADZADEH A, SHALCHI-AMIRKHIZ B, MOHAMMADI M, HAGSHENAS M. Post heat treatment of additive manufactured AlSi10Mg: On silicon morphology, texture and small-scale properties [J]. Materials Science and Engineering A, 2020, 783: 139296.
[44] YUE H, CHEN Y, WANG X, XIAO S, KONG F. Microstructure, texture and tensile properties of Ti−47Al−2Cr−2Nb alloy produced by selective electron beam melting [J]. Journal of Alloys and Compounds, 2018, 766: 450−459.
[45] LI X, YI D, WU X, ZHANG J, YANG X, ZHAO Z, FENG Y, WANG J, BAI P, LIU B. Effect of construction angles on microstructure and mechanical properties of AlSi10Mg alloy fabricated by selective laser melting [J]. Journal of Alloys and Compounds, 2021, 881: 160459.
[46] SOUNDARARAJAN R, RAMKUMAR K R, SIVASANKARAN S, KIM H S. Enhancement of tensile strength in AA 6061-T6 plates joined by gas tungsten arc welding using high entropy alloy filler sheet [J]. Materials Science and Engineering A, 2022, 832: 1−9.
[47] LIU X, ZHAO C, ZHOU X, SHEN Z, LIU W. Microstructure of selective laser melted AlSi10Mg alloy [J]. Materials & Design, 2019, 168: 107677.
[48] LI R, CHEN H, ZHU H, WANG M, CHEN C, YUAN T. Effect of aging treatment on the microstructure and mechanical properties of Al−3.02Mg−0.2Sc−0.1Zr alloy printed by selective laser melting [J]. Materials & Design, 2019, 168: 107668.
[49] SIVASANKARAN S, AL-MUFADI F. Influence of strain rate and percentage of cold work on room-temperature deformation behaviour of AISI 1015 carbon steel: Detailed microstructures and cold workability map investigations [J]. Transactions of the Indian Institute of Metals, 2020, 73: 1439−1448.
[50] SIVASANKARAN S, RAMKUMAR K R, AMMAR H R, AL-MUFADI F A, ALABOODI A S, IRFAN O M. Microstructural evolutions, hot deformation and work hardening behaviour of novel Al−Zn Binary alloys processed by squeezing and hot extrusion [J]. Metals and Materials International, 2022, 28: 998−1013.
[51] HADADZADEH A, SHALCHI AMIRKHIZ B, ODESHI A, LI J, MOHAMMADI M. Role of hierarchical microstructure of additively manufactured AlSi10Mg on dynamic loading behavior [J]. Additive Manufacturing, 2019, 28: 1−13.

直接时效对铸造与选区激光熔化 AlSi10Mg 合金的显微组织、力学性能及强化机理的影响

A. SATHISHKUMAR [1], R. SOUNDARARAJAN [1], S. SIVASANKARAN [2], A. RAMESH [3]

1. Department of Mechanical Engineering, Sri Krishna College of Engineering and Technology, Coimbatore, India;
2. Department of Mechanical Engineering, College of Engineering, Qassim University, Buraydah 51452, Saudi Arabia;
3. Department of Mechanical Engineering, Chennai Institute of Technology, Chennai, India

摘　要：研究了直接时效(DA)热处理对铸造和选区激光熔化(SLM)AlSi10Mg 合金显微组织和力学性能的影响。SEM 和 EBSD 显微组织表征显示，SLM 合金具有细晶胞状组织，含 α(Al)和富 Si 相，而铸造合金具有粗大的共晶 Si 形貌。后续的直接时效热处理对力学性能的提升效果显著，与未经热处理的 SLM AlSi10Mg 合金(NHT-AB)相比，热处理后合金(DA-B)的屈服强度提高了 9.24%，极限抗拉强度提高了 5.56%。断口形貌分析表明，SLM 合金主要表现为韧性断裂，而铸态合金则表现为韧−脆混合式断裂。此外，EBSD 织构分析表明，拉伸变形后，SLM 合金颈区的晶粒被拉长。析出强化对 SLM 合金强度提高的贡献最大，其次是晶界强化。这些发现突显了 SLM 和 DA 工艺制造的高性能 AlSi10Mg 零件在航空航天、汽车和快速成型等应用领域的潜力。

关键词：AlSi10Mg 合金；选区激光熔化；直接时效；力学性能；强化机理； EBSD 织构分析

(Edited by Bing YANG)